



Temporal fine structure of all-normal dispersion fiber supercontinuum pulses caused by non-ideal pump pulse shapes

ANUPAMAA RAMPUR,^{1,*} DIRK-MATHYS SPANGENBERG,²
GRZEGORZ STĘPNIEWSKI,^{1,3} DOMINIK DOBRAKOWSKI,¹ KAROL
TARNOWSKI,⁴ KAROLINA STEFAŃSKA,⁴ ADAM PAŹDZIOR,⁵ PAWEŁ
MERGO,⁵ TADEUSZ MARTYNIEN,⁴ THOMAS FEURER,² MARIUSZ
KLIMCZAK,¹ AND ALEXANDER M. HEIDT²

¹University of Warsaw, Faculty of Physics, Pasteura 5, 02-093 Warsaw, Poland

²Institute of Applied Physics, University of Bern, Sidlerstrasse 5, 3012 Bern, Switzerland

³Institute of Electronic Materials Technology, Glass Department, Wólczyńska 133, 01-919 Warsaw, Poland

⁴Department of Optics and Photonics, Wrocław University of Science and Technology, Wybrzeże
Wyspiańskiego 27, 50-370 Wrocław, Poland

⁵Laboratory of Optical Fiber Technology, Maria Curie-Skłodowska University, pl. M. Curie-Skłodowskiej
3, 20-031 Lublin, Poland

*anupamaa.rampur@fuw.edu.pl

Abstract: We experimentally investigate the spectro-temporal characteristics of coherent supercontinuum (SC) pulses generated in several implementations of silica and soft-glass all-normal dispersion (ANDi) photonic crystal fibers optimized for pumping with Erbium (Er):fiber femtosecond laser technology. We characterize the resulting SC using time-domain pychography, which is especially suitable for the measurement of complex, spectrally broadband ultrashort pulses. The measurements of the ANDi SC pulses reveal intricate pulse shapes, considerable temporal fine structure, and oscillations on time scales of < 25 femtoseconds, which differ from the smoothness and simplicity of temporal profiles obtained in numerical simulations and observed in previous experiments. We link the measured complex features to temporal sub-structures of the pump pulse, such as pre- and post-pulses and low-level pedestals, which are common in high pulse energy ultrafast Er: fiber systems. We also observe spectro-temporal structures consistent with incoherent noise amplification in weakly birefringent fiber samples. Our results highlight the importance of the pump source and polarization-maintaining (PM) fibers for high-quality SC generation and have practical relevance for many ultrafast photonics applications employing ANDi fiber-based SC sources.

© 2020 Optical Society of America under the terms of the [OSA Open Access Publishing Agreement](#)

1. Introduction

Optical fibers with engineered, normal chromatic dispersion characteristics take a special place in ultrafast fiber optics due to their applications in chirp management in mode-locked fiber laser oscillators [1] and in coherent SC generation [2]. In nonlinear fiber optics, normal dispersion fibers bring the advantage of suppressing modulation instability and Raman effect at sufficiently short pulse durations [3], which are associated with quantum noise amplification in the anomalous dispersion region [4]. Therefore, fibers exhibiting ANDi profiles are capable of producing spectrally broadband and coherent SC over a wide range of pump pulse parameters [3,5]. Light pulses with spectra spanning a full octave, obtained in ANDi fibers pumped with femtosecond Titanium:Sapphire lasers, have been compressed down to the single optical cycle regime [6], and have also been used as seed signal for high repetition rate single-cycle optical parametric chirped-pulse amplifier systems [7], enabling high harmonics generation and isolated attosecond

pulse generation at high average powers [8]. Broadband and temporally uniform ANDi SC pulses in the near-infrared, pumped by ultrafast Ytterbium: fiber lasers, have found applications in various fields of ultrafast photonics, e.g. nonlinear bio-photonics imaging, micro-spectroscopy, optical coherence tomography, and multidimensional ultrafast spectroscopy [9–12]. Using fibers made from chalcogenide glasses and using optical parametric amplifiers as pump source, several implementations of ANDi SC sources with spectral coverage in the mid-IR up to 12 μm have recently been demonstrated for application in vibrational spectroscopy [13,14]. However, especially promising is the combination of ANDi fibers with femtosecond pump sources based on Erbium- (Er): fiber technology as this allows the construction of compact and robust all-fiber coherent SC sources [15,16]. Applied as a broadband coherent seed, such systems have recently formed the basis for the realization of ultra-low noise frequency combs and ultrafast fiber amplifier systems in the 2 μm spectral range [17–19].

Many of these applications benefit from SC with uniform and smooth spectral and temporal intensity profiles. ANDi SC pulses are often assumed to fulfill these requirements, backed up by many numerical simulations available in literature covering various fiber designs and pump wavelengths (e.g. [14,15,20–23]). However, detailed experimental data on the spectro-temporal characteristics of ANDi SC pulses is scarce [24,25], yet such measurements are necessary to evaluate the properties of ANDi SC and its suitability for specific applications under real pumping conditions. In contrast to numerical simulations, which typically assume ideal Gaussian or hyperbolic secant pulse shapes, femtosecond pulses emitted by real lasers often exhibit imperfections. While it is known that non-ideal pulse shapes can have a significant effect on the spectro-temporal properties of the generated ANDi SC [26], their impact has not been assessed experimentally so far. The often complex spectro-temporal correlations of SC pulses can be conveniently visualized using spectrograms created via cross-correlation optical gating. The analysis of such experimentally recorded or numerically simulated spectrograms has contributed significantly to the understanding of the nonlinear dynamics involved in SC generation under various pumping conditions [3,27–29]. More recently, measurements of spectrograms have been used to optimize fiber SC generation for specific applications [30], for dispersion measurements of birefringent photonic crystal fibers (PCF) [31], and for the characterization of optical rogue waves [32].

In this work, we report the detailed experimental spectro-temporal characterization of coherent SC pulses generated in several implementations of microstructured ANDi PCF pumped by a commercial ultrafast Er: fiber amplifier system. The PCF were drawn using either highly nonlinear silicate soft glasses or germanium-doped and pure silica glass, and their dispersion was specifically engineered to realize ANDi profiles at the pump wavelength of 1560 nm. Both PM and non-PM fibers are investigated. Experimental spectrograms were recorded and analyzed using time-domain ptychography (TDP) [33], which has proven especially suitable for the characterization of complex and spectrally broadband ultrashort pulses [34–36]. Our measurements reveal that the SC pulses emitted from all the investigated ANDi PCF exhibit intricate pulse shapes, a considerable amount of temporal fine structure, and fast oscillations on the scale of tens of femtoseconds. These results differ from the relative smoothness and simplicity of the temporal envelope typically obtained in numerical simulations and observed in previous experiments using fundamental solitons as pump source [25]. We trace the origin of these observed complex features to imperfections of the pump pulse, such as side pulses and low-level pedestals, which are common in high energy femtosecond Er: fiber amplifier systems [37]. We also observe spectro-temporal structures of SC pulses generated in weakly birefringent fiber samples that are consistent with signatures of incoherent noise amplification due to polarization modulation instability (PMI) and the nonlinear coupling of parametric four-wave mixing (FWM) and stimulated Raman scattering (SRS) discussed in recent numerical studies [3,38]. These results highlight the importance of the pump source and highly birefringent, PM fibers for

high-quality SC generation and provide important guidance for the design and application of ANDi SC sources in ultrafast photonics.

2. Optical properties of used PCFs

In this work we use two different types of microstructured ANDi PCF: (i) all-solid silicate glass PM and non-PM PCFs developed at the Institute of Electronic Materials Technology (ITME) in Warsaw; and (ii) silica/Ge:silica core PM PCFs developed at the Laboratory of Optical Fiber Technology, Maria Curie-Skłodowska University in Lublin, Poland. In total we investigate five different fiber designs, their lineup is shown in Fig. 1 with their chromatic dispersion measured using a balanced Mach-Zehnder interferometer [39,40], microstructure images recorded using scanning electron microscopy (SEM), and a typical SC spectrum generated in an approx. 10 cm long piece of each PCF. SC were generated using a commercially available Er:fiber-based laser (Menlo Systems C-fiber HP), operating at a central wavelength of 1560 nm, with a 100 MHz repetition rate, delivering 75 fs pulses with an average power of 350 mW, which corresponds to around 40 kW of peak power. A summary of linear and nonlinear optical properties, as well as geometric parameters of the fibers used in this work, is given in Table 1.

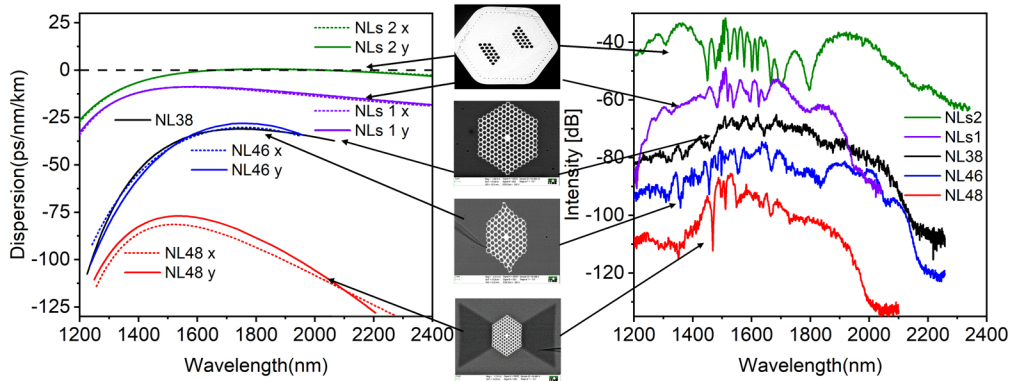


Fig. 1. Chromatic dispersion of PM and non-PM ANDi PCFs used in this work (left) along with scanning electron microscopy pictures (center) and respective typical supercontinuum spectrum (right) marked with arrows and labels.

In the class of PCF drawn from highly nonlinear silicate soft glasses, we firstly investigate a non-PM, all-solid PCF labeled NL38. Its properties and SC generation performance were previously described in detail [41,42]. In brief, this design was realized using two commercially available and thermally compatible silicate glasses. Schott SF6 glass was used as the core and photonic lattice glass, Schott F2 glass was used to fill the lattice inclusions as well as for the outer cladding tube. This all-solid glass PCF approach facilitates the engineering of flattened ANDi profiles as shown in Fig. 1, and a typical SC generated in this fiber spans from approx. 1100 - 2100 nm. Keeping NL38 as a base design, two PM designs were realized by introducing either form- or stress-induced birefringence [43]. In one variant involving the elliptical deformation of the fiber structure, labeled NL46, the core was squeezed along one of the axes as shown in Fig. 1, which gives rise to group birefringence of 4.38×10^{-4} measured at a wavelength of 1900 nm. The chromatic dispersion and SC broadening in this fiber are very similar to NL38. In a second PM version, labeled NL48, a bow-tie structure replaced the outer ring of the all-solid glass honeycomb-like cladding. Stress birefringence was introduced by fabricating the bow-tie structure from a modified F2-based glass composition with a significantly increased thermal expansion coefficient compared to F2 [43]. The modified structure has similar group birefringence

Table 1. Geometry, linear and nonlinear properties of the photonic crystal fibers used in this work.

Fiber label and glass types	Core / photonic cladding dimensions (μm)	Local maximum of dispersion (x and y axis in case of PM)	Zero dispersion wavelengths	Measured group birefringence at 1900 nm	Estimated nonlinear coefficient γ (1/W/km)	Ref.
NL38, F2/SF6 all-solid glass PCF	2.57×2.57 / 27.64×24.19	-31.0 ps/nm/km, 1724 nm	None within transmission window	-	125 (2000 nm)	[41,43]
NL46, F2/SF6 all-solid glass PCF with elliptical microstructure	2.68×1.91 / 25.8×16.3	-51.7 ps/nm/km, 1645 nm, -56.3 ps/nm/km, 1653 nm	None within transmission window	4.38×10^{-4}	122 (2000 nm)	[41,43]
NL48, F2/SF6 all-solid glass PCF with stress areas	2.5×2 / 24.54×18.66	-76.9 ps/nm/km, 1533 nm, -81.3 ps/nm/km, 1520 nm	None within transmission window	3.74×10^{-4}	113 (2000 nm)	[41,43]
NLs1, silica, Ge:silica, squeezed lattice air-hole PCF	1.69×1.41 / 54×62	-8.75 ps/nm/km, 1591 nm, -8.89 ps/nm/km, 1572 nm	None within transmission window	1.65×10^{-5}	4 (2000 nm)	[44]
NLs2, silica, Ge:silica, squeezed lattice air-hole PCF	1.69×1.61 / 33×49	0.64 ps/nm/km, 1834 nm 0.52 ps/nm/km, 1825 nm	Around 1670 nm and 2050 nm	4.46×10^{-5}	4 (2000 nm)	[44]

of 3.74×10^{-4} measured at 1900 nm, but it has normal chromatic dispersion with much higher absolute values than the NL38 and NL46 designs. This results in reduced spectral broadening during SC generation as shown in Fig. 1.

The second class of PCF used in this work comprised two designs of microstructured silica fibers with an elliptically shaped, germanium-doped core and birefringence induced by squeezed lattice labeled NLs1 and NLs2, shown in Fig. 1 [44]. The measured group birefringence was around 1.65×10^{-5} and 4.46×10^{-5} for NLs1 and NLs2, respectively. The NLs1 fiber has an almost perfectly flat ANDi profile, but compared to the lead-silicate PCF the spectral broadening during SC generation is reduced due to a significantly smaller nonlinearity of the base glass and a reduced modal confinement at long wavelengths [45]. The second fiber, labeled NLs2, exhibits effectively zero dispersion over a very wide wavelength span around 1600 - 2200 nm. The dispersion measurement with the balanced Mach-Zehnder interferometer yields a local maximum of 0.64 ps/nm/km (± 0.1 ps/nm/km) at 1834 nm and two zero-dispersion wavelengths (ZDWs) around 1660 nm and 2050 nm. The error of the ZDW positions in the dispersion measurement is approx. ± 12 nm. The measured SC spectrum is the broadest of all investigated fibers and reaches up to 2300 nm, and exhibits quite different, more pronounced spectral features compared to the other fibers in this work. Despite the dispersion measurement uncertainty, the change of sign of the dispersion profile in this fiber is later confirmed with a characteristic, curved SC group delay trace obtained experimentally (Section 5.3).

3. Experimental setup

The spectro-temporal characterization of the SC pulses was performed using TDP [33]. The required spectrograms for ptychographic reconstruction of the pulses are recorded with the use of a standard, in-house built sum-frequency generation based cross-correlation optical gating setup shown in Fig. 2 [27,35,36,46,47]. As the pump source, we used a commercially available Er:fiber-based laser (Menlo Systems C-fiber HP), as described in the previous section. The pump

signal was split into two beams with a 90:10 ratio beam splitter (BS). The 90% part of the pulse energy was used to pump SC generation in the PCF, while the other 10% was used as gate pulse.

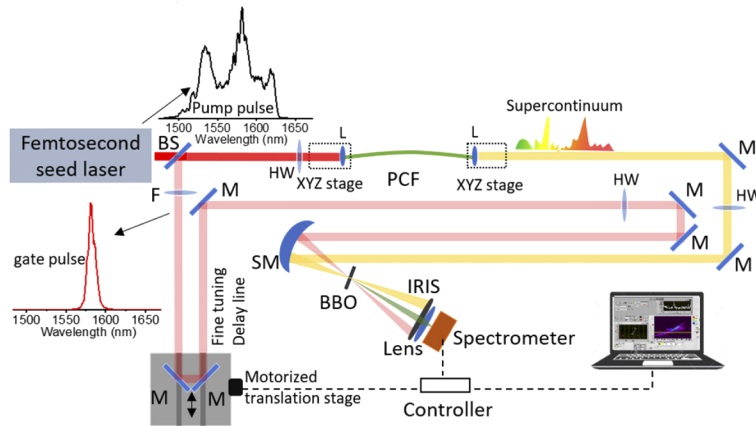


Fig. 2. Experimental setup for ptychographic pulse characterization: femtosecond seed laser: 1560 nm, 100 MHz, 350 mW, 75 fs (Menlo Systems C-fiber HP); BS: beam splitter; F: 1580 nm bandpass filter; PCF: photonic crystal fiber; M: highly reflective mirror; HW: half-wave plate; L: aspheric lens; SM: spherical mirror; BBO: β -barium borate crystal.

The femtosecond pump laser spectrum is depicted in Fig. 2 in the pump arm. The light was coupled into the fibers through an aspheric lens with a focal length of 4 mm and an anti-reflection coating compatible with the pump laser spectrum. The coupling efficiency estimated based on the ratio of the incident pump power to the SC output average power and considering the attenuation of the used fiber section, was in the case of the silicate PCFs labelled NL46, NL38, and NL48 around 46%, 36%, and 26%, respectively, while in the silica PCFs labelled NLs1 and NLs2 it was around 65%. In the case of the PM fibers, a 1560 nm half-wave plate was used to match the linearly polarized pump pulses to one of the principal axes of the fibers. The PCFs were mounted onto a 3-axis translation stage for precise control of the input condition. The generated SC is collimated using an outcoupling lens. A polarizer was placed at the output of these PCFs to assess the state of polarization of light exiting the fibers and to verify the PER in the generated SC pulses. An optical spectrum analyzer (OSA, operating wavelength 1200 -2400 nm) was used to record independent SC spectra required to correct the measured spectrograms. Due to small differences in chromatic dispersion profiles between the two principal axes of the PM fibers, the widths of SC spectra were slightly different for either of the principal axes in a given PCF. During the experiments, pump pulse polarization was aligned with the PCF axis enabling the broader SC spectrum at the output, and this was done by proper adjustment of the half-wave plate at the PCF input.

The gate pulse is formed by filtering 10% of energy from the pump pulse using a 14 nm bandpass filter with 1580 nm central wavelength, which coincides with the main peak of the pump spectrum. In comparison to the unfiltered pump pulse, the filtered gate pulse with its quasi-Gaussian spectrum results in much simpler and cleaner spectrograms, facilitating their interpretation and reconstruction. Note that in TDP the obtainable temporal resolution is independent of the gate pulse duration such that the spectral filtering does not result in the loss of any information [33,36]. A motorized piezo-driven delay stage is used for precise control of the time delay between gate pulse and SC pulse.

The spectrally broad and chirped SC pulse from the PCFs and the filtered gate pulse were focused on the BBO crystal by a spherical mirror. Here we used a 0.5 mm β -barium borate crystal (BBO) with type I phase-matching for sum-frequency generation (SFG). The SFG signal

was recorded as a function of the time-delay between SC and gate pulse using a compact Czerny-Turner spectrometer (Ocean Optics, 350–1000 nm sensitivity range, 2.0 nm resolution). The polarization state of both pulses was controlled with broadband half-wave plates. Any unconverted SC and reference pulse light transmitted through the BBO crystal was filtered with an iris before the spectrometer. The large phase-matching bandwidth required to generate a SFG signal for all frequencies contained in the SC pulse is a challenge that was addressed by recording three spectrograms with different BBO tuning angles and overlapping them in order to obtain a SFG signal with sufficient signal-to-noise ratio at the extremes of the SC spectrum. The measured spectrograms were corrected for all frequency-dependent effects, including the BBO phase-matching efficiency, by comparing the spectral marginal to the cross-convolution of independently measured SC and probe pulse spectra and enforcing agreement of these two quantities [48]. Standard background correction and noise filtering were applied.

We employed the extended ptychographic iterative engine (e-PIE) for the extraction of the full amplitude and phase information of both the SC pulse and the gate pulse simultaneously from a single spectrogram [34,36].

4. Characterization of pump laser pulse and gate pulse

We characterize both pump and gate pulses using second-harmonic frequency-resolved optical gating (SHG-FROG) and a retrieval algorithm based on generalized projections [46,49]. The pump pulse temporal amplitude and phase are required as input for numerical simulations described in Section 5.1, while the measurement of the gate pulse serves as an additional independent measure of accuracy for the subsequent, more demanding SC spectrogram reconstructions using e-PIE. As the e-PIE algorithm reconstructs both SC pulse and gate pulse, we can then easily determine the accuracy and convergence of the reconstruction by ensuring equivalence of e-PIE and SHG-FROG results for the gate pulse.

The results for the pump laser are shown in Fig. 3. The retrieved spectrogram accurately reproduces the experimental data with an error of 1.9×10^{-3} . The temporal and spectral full width at half maximum (FWHM) of the pump pulse were determined to 75.3 fs and 92 nm, respectively.

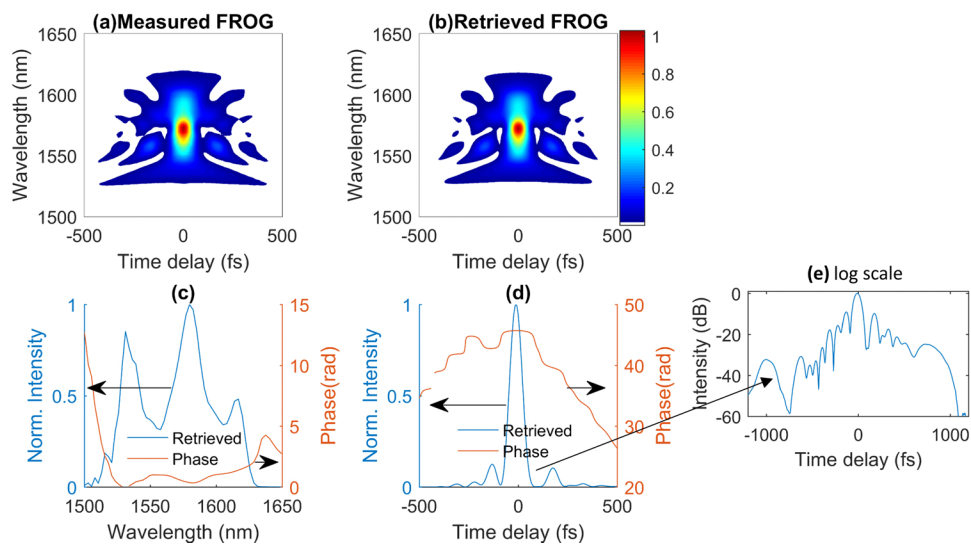


Fig. 3. Characterization of the pump pulse using SHG FROG. (a) Measured FROG trace, (b) retrieved FROG trace, (c) retrieved spectrum (blue) and phase (orange), (d) retrieved pulse shape (blue) and phase (orange), and (e) temporal intensity in logarithmic scale.

The pump pulse also displays pre- and post-pulses with peak intensities of about 10% of the main pulse, and a pedestal on the -20 dB level especially pronounced on the trailing edge of the pulse reaching out to about 1 ps, as highlighted in the logarithmic scale plot in Fig. 3. Such features are common in high pulse energy, sub-100 fs Er:fiber amplifier systems [37]. The roles of this pedestal and the side pulses in SC pulse formation are discussed in detail in the following section, using experimentally obtained SC pulse data and nonlinear propagation simulations taking into account measured pump pulse data shown in Fig. 3.

The SHG-FROG results for the gate pulse filtered with the 1580 nm bandpass filter are shown in Fig. 4. The retrieval error was 1.1×10^{-3} . The gate pulse had 337.5 fs FWHM duration and a 14 nm spectral width. Evidently, the spectral filtering removed side pulses and low-level pedestal, and both temporal and spectral shape are quasi-Gaussian. Hence, the filtered pulses are more suitable for use as gate pulses as they generate visually much clearer cross-correlation spectrograms, in which any complex features can uniquely be attributed to the SC pulse. In addition, the longer gate pulse duration does not have any negative impact on the obtainable temporal resolution of the TDP technique [33,36].

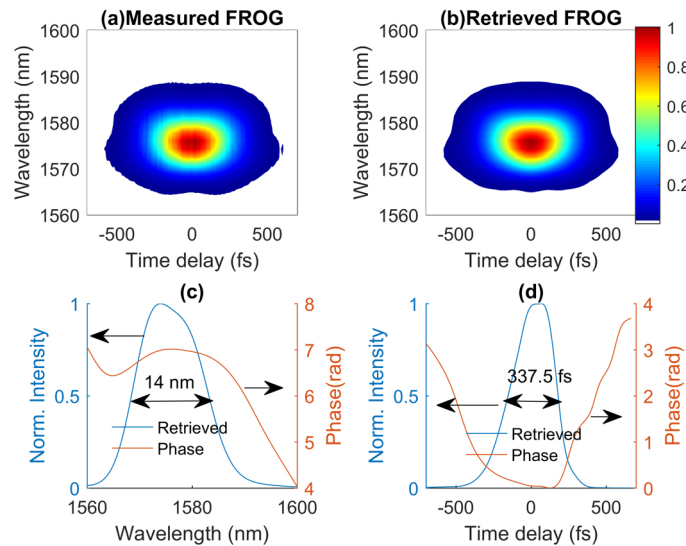


Fig. 4. Characterization of the gate pulse after the bandpass filter using SHG FROG. (a) Measured FROG trace, (b) retrieved FROG trace, (c) retrieved spectrum (blue) and phase (orange), (d) retrieved pulse shape (blue) and phase (orange).

5. Spectro-temporal characterization of SC pulses

5.1. Soft-glass PCF: NL46 fiber (PM)

We first characterize the SC pulses generated in NL46 PM PCF using a 10.4 cm long sample. Figure 5 summarizes the measurement results and the excellent quality of the pulse retrieval achieved by the e-PIE algorithm. All intricate details of the measured spectrogram shown in Fig. 5(a) are very well reproduced in the retrieved spectrogram shown in Fig. 5(b), resulting in minimal errors not exceeding $\pm 0.2\%$ across the entire, nearly octave-spanning width of the SC pulse spectrum as shown in Fig. 5(c). The high fidelity of the reconstruction is underlined by the excellent agreement of the retrieved spectrum with an independently measured SC spectrum using the OSA, as shown in Fig. 5(d).

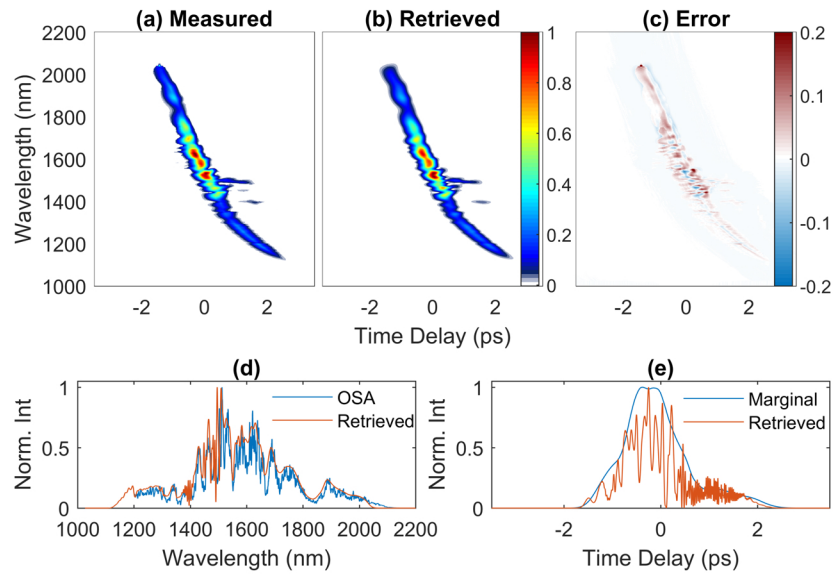


Fig. 5. Spectro-temporal characterization of SC pulses generated in the NL46 PCF. (a) Measured spectrogram. (b) retrieved spectrogram using e-PIE. (c) Error calculated by subtracting (a) from (b). (d) Retrieved spectrum compared to a SC spectrum independently measured with the OSA (linear scale). (e) Retrieved temporal pulse shape with marginal.

The general shape of the spectrogram confirms nonlinear broadening dynamics typical for SC generation in normal dispersion fibers under femtosecond pumping, which are dominated by self-phase modulation (SPM) and optical wave breaking (OWB), preserving the temporal integrity of the SC pulse [2,5]. In our pumping conditions the optical wave breaking length scale (L_{WB}) is < 1 cm in this fiber, i.e. SC generation dynamics are concluded and the spectrum fully developed at the exit of our fiber sample [2]. L_{WB} is of similar magnitude also in the other investigated soft-glass PCF discussed below. This also supports the selection of the fiber sample length, which is longer, than the length required for the SC broadening process to complete. We note however, that the roughly 10 cm sample length selected for this and the following experiments in this work, was also motivated by convenience of handling. Going back to the group delay characteristics shown in Fig. 5, it can be observed, that the chirp of the SC pulse is positive and predominantly linear from 1300 nm to 2100 nm.

Figure 5(e) shows the SC pulse shape retrieved by e-PIE, which is characterized by substantial modulation, fine structure and fast oscillations on time scales much shorter than the original pump pulse. In contrast, in the temporal marginal, which is directly accessible from the spectrogram measurement, these features are masked since any structure shorter than the gate pulse duration (340 fs) cannot be resolved, i.e. ptychographic pulse reconstruction is required to reveal these temporal details. The modulated pulse shape and the complex features observed in the spectrogram differ considerably from the smoothness and simplicity typically obtained in numerical simulations (e.g. [2,14,15,20–23]), and also observed in previous spectro-temporal characterizations of ANDi SC pulses [5,25].

Since similar temporal fine structure was observed in all investigated fibers in this work, as discussed in the following sections, we performed numerical simulations in order to clarify the origin of these features. The simulation is based on the generalized nonlinear Schrödinger equation (GNLSE) [50,51] using the measured dispersion profile and nonlinear properties of NL46 given in Fig. 1 and Table 1, as well as the real pump pulse amplitude and phase obtained

from the FROG measurements [Fig. 3(d)]. Since this fiber is polarization-maintaining with a relatively large birefringence (see Table 1), a single-polarization, single-mode GNLSE version is employed.

In Figs. 6(a) and 6(b) the measured and simulated spectrograms are compared. The projected spectral and temporal axes shown in Fig. 6(a) are retrieved by TDP and in Fig. 6(b) is simulated by GNLSE. The simulation is able to reproduce the observed complexity of the spectrogram and temporal profile very well, which also serves as an additional independent confirmation for the validity of the ptychographic pulse reconstruction. Minor differences between simulated and measured spectrograms are attributed to uncertainties of the measured fiber properties and the propagation of the measured SC pulse through several dispersive optical elements after exiting the fiber. The shortest temporal features in both measured and simulated temporal pulses are oscillations at time delays of 0.8-1.2 ps shown in the insets. These fast oscillations are due to the beating caused by the temporal overlap of the SC spectrum with a long and spectrally narrow feature around 1530 nm. Using the simulation, this feature can be traced back to the unconverted low-level pedestal of the pump pulse, which was identified in the characterization of the pump pulse in Section 4 and is well visible in Fig. 3(e). The beat frequency is equal to the spectral separation of pump pedestal and overlapping SC spectrum, which from the spectrogram can be determined to be ~ 40 THz. The spectral resolution for all the recorded spectra was 2 nm. The resulting oscillation period retrieved using TDP is 25 fs, which matches well with the simulated results.

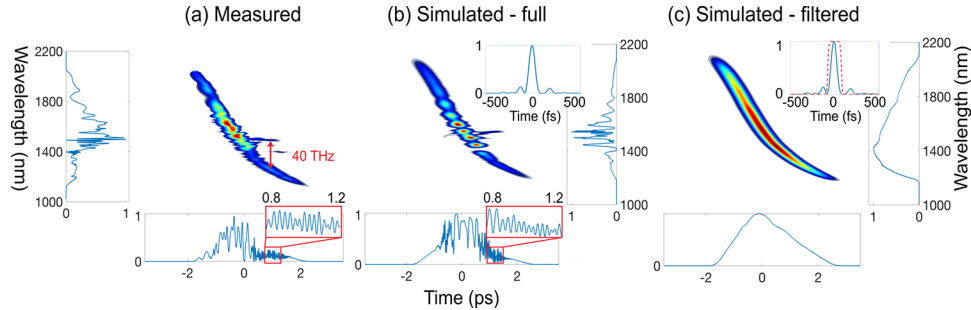


Fig. 6. Projected axes spectrograms of SC pulses generated in NL46 PCF. (a) Measured; (b) simulated considering full amplitude and phase of measured pump pulse; (c) simulated considering temporally filtered pump pulse without side-peaks or pedestal. The projected axes show the retrieved or simulated spectral and temporal profiles, respectively, both in linear scale. Top insets in (b) and (c) show the pump pulse shape considered in the respective simulations.

In fact, most of the observed modulation and fine structure of the SC pulse in both spectral and temporal domains can be traced back to the pump pulse. In Fig. 6(c) we repeat the simulation using exactly the same parameters, but we apply a super-Gaussian filter to the measured pump pulse isolating the main peak and suppressing side pulses and pedestal. In this way, all the complexity disappears, and the smooth temporal and spectral profiles usually associated with ANDi SC can be recovered. Hence, the non-ideal pulse shape emitted by the Er: fiber pump laser can be clearly identified as the origin of the temporal (and spectral) fine structure of the SC pulse observed in our measurements.

We note that there is a low-level noisy feature in the measured spectrogram at coordinates of approx. 1400 nm / +1-2 ps, which is not reproduced by the simulation. This proves that this feature cannot be explained by single-polarization nonlinear dynamics. Instead, in Section 5.2 we link this feature to the occurrence of PMI, which is associated to the depolarization of the SC pulse.

5.2. Soft-glass PCF: NL48 (PM) and NL38 (non-PM) fiber

Figure 7(a) shows the measured spectrogram of the SC pulse generated in a 10.1 cm sample of NL48 PM PCF. The spectral projection contains the spectrum retrieved by e-PIE compared to an independent OSA measurement, confirming a high fidelity pulse reconstruction. The temporal projection displays the marginal of the spectrogram as well as the intensity and phase retrieved by e-PIE. The temporal modulation and beating effects due to the non-ideal pump pulse shape discussed above for the NL46 fiber are also clearly visible. The pulse duration is longer (5.9 ps) and the spectrum narrower compared to the measurements using the other soft-glass PCF, which is in agreement with the stronger chromatic dispersion of the NL48. The spectrogram also highlights an almost perfect linear chirp of the pulses without significant higher-order contributions. This feature could prove useful, e.g. in fiber-based ultrafast chirped-pulse amplification using the SC pulse as seed source [17–19].

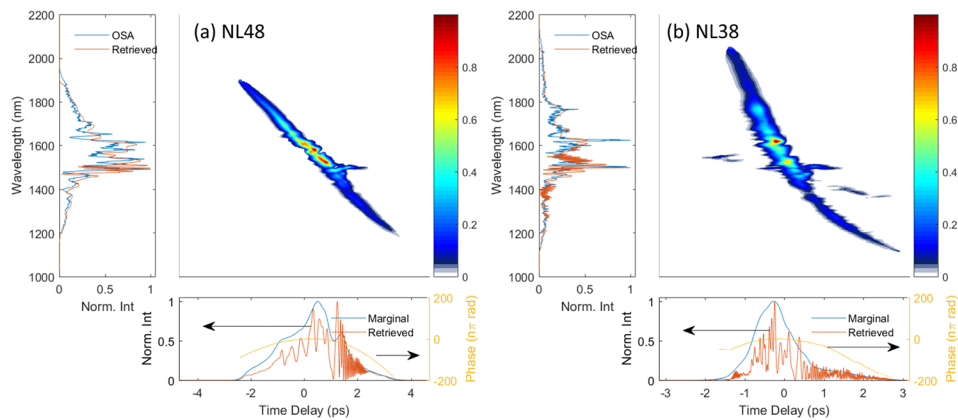


Fig. 7. Measured projected axes spectrograms of SC pulses generated in soft-glass PCF. (a) NL48 – polarization maintaining. (b) NL38 – non-polarization maintaining. The spectral projection displays the spectrum retrieved by e-PIE compared to an independent OSA measurement (linear scale). The temporal projection displays the marginal of the spectrogram as well as the intensity and phase retrieved by e-PIE.

We performed similar spectro-temporal characterization measurements with a 14.4 cm sample of NL38, which is non-PM. The slightly increased sample length in the case of NL38 served again convenience of handling, as well as preserving the available sample. We note that the slightly longer sample in comparison to NL46 is not expected to significantly change the contribution of incoherent nonlinear effects. According to previous studies, in order to observe qualitative change of pulse distortions, i.e. due to stimulated Raman scattering, the fiber sample length would have to be increased into the order of 1-2 m in our pumping conditions [3,38]. The results are shown in Fig. 7(b). With this fiber we observe considerably more fine structure in both spectral and temporal domains than with the corresponding PM fibers. The spectrogram trace of the main pulse is not as well defined as in the case of highly birefringent fibers and exhibits quite noisy contour lines. Additionally, spectral and temporal beating effects are caused by the appearance of low-level features at wavelength / delay coordinates of around 1600 nm / -2 ps and 1400 nm / +1-2 ps. These features were not observed in fibers with high birefringence. It was recently shown that nonlinear dynamics in ANDi fibers with weak or unintentional birefringence are much more susceptible to quantum noise amplification by PMI, while this effect is suppressed in highly-birefringent PM fibers [38,52]. Hence, we believe that the noisy contour of the main trace in the spectrogram and the additional low-level features are signatures for the onset of noise

amplifying nonlinear dynamics due to PMI and the nonlinear coupling of FWM and SRS, as similarities exist with the simulated evolution of such dynamics presented in Ref. [3].

Interestingly, a similar low-level noisy feature at the coordinates 1400 nm / +1-2 ps was also observed in the spectrogram measurements of the SC pulse generated in the NL46 fiber (Figs. 5 and 6), which is the PM version of NL38. In contrast, the noisy feature at 1600 nm / -2 ps is absent in NL46. Detailed wavelength-dependent birefringence measurements of NL46 show that the birefringence drops to zero around 1400 nm such that noise amplification by PMI is indeed possible [43]. On the other hand, at 1600 nm NL46 exhibits a birefringence of approx. 1×10^{-4} [43], effectively suppressing PMI. These observations provide further evidence that the observed low-level noisy features are indeed caused by nonlinear dynamics related to PMI.

5.3. Silica/Ge:silica PM PCF: NLs1 and NLs2

The silica PCF exhibit much lower nonlinearity than the tested soft-glass PCF, as shown in Table 1. This is partly offset by a remarkably low loss estimated below 0.1 dB/m around 1.75 μm [44] (compared to about 20 dB/m in the case of the soft-glass PCF) as well as weaker and flatter dispersion (Fig. 1). The latter facilitates spectral broadening and efficient transfer and of energy from the central pump wavelength to the SPM and OWB sidebands [20]. In addition, fibers with low chromatic dispersion avoid excessive pulse broadening and maintain high peak powers for longer propagation distances. Therefore, the silica PCF in this work produce SC spectral bandwidths comparable to the investigated soft-glass PCF.

The spectro-temporal measurements of both investigated silica PCF are summarized in Fig. 8. To be directly comparable with the soft-glass PCF measurements, the spectrogram traces, spectra, and pulse shapes for these fibers were obtained for approx. 10 cm long samples. Both fibers emit much shorter SC pulses than the investigated soft-glass PCF, the measured pulse durations are below 0.5 ps. Such pulses with broad spectral bandwidth and low chirp values are convenient for ultrafast applications, e.g. for nonlinear imaging or compression to few-cycle pulse durations. However, it is also evident from these measurements that any imperfections of the pump pulse are directly translated to the SC pulse, such as the unconverted low-level pedestal at 1530 nm which is very prominent in both measurements in Fig. 8.

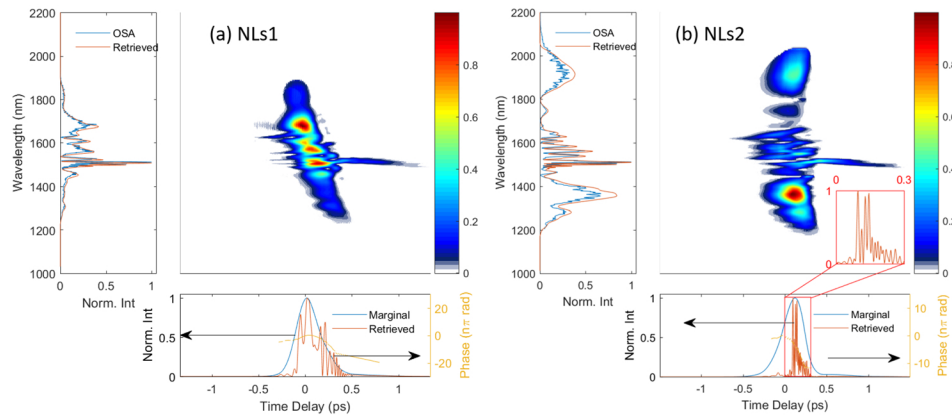


Fig. 8. Measured projected axes spectrograms of SC pulses generated in polarization-maintaining silica PCF. (a) NLs1. (b) NLs2. The spectral projection displays the spectrum retrieved by e-PIE compared to an independent OSA measurement (linear scale). The temporal projection displays the marginal of the spectrogram as well as the intensity and phase retrieved by e-PIE. The inset in (b) shows a magnified section of the temporal intensity profile.

The NLs1 fiber exhibits all-normal chromatic dispersion, leading to a positive, practically linear chirp across the SC spectrum [Fig. 8(a)]. L_{WB} in this fiber is estimated to ~ 7 cm, i.e. comparable to the length of the fiber sample. Consequently, the spectrum would slightly broaden and flatten with increased fiber length. Nevertheless, it is clear that spectral broadening is reduced compared to the soft-glass PCF as the dispersion is not quite low enough to completely offset the lower glass nonlinearity.

This is different in the case of the NLs2 fiber [Fig. 8(b)]. The very low, near-zero dispersion profile of this fiber facilitates spectral broadening equivalent to the investigated soft-glass PCF. According to the measured dispersion profile displayed in Fig. 1, the fiber exhibits very low anomalous dispersion in the range 1650–2050 nm. This is confirmed by the change of slope of the spectrogram trace around 1650 nm. The low absolute value of chromatic dispersion leads to a temporal overlap of spectrally widely separated components, resulting in high-frequency temporal beating with peak durations of ~ 6 to 8 fs (retrieved using TDP), as seen in the inset of Fig. 8(b). The spectrogram is dominated by two broad peaks located at 1350 nm and 1900 nm. Simulations confirm that both peaks are generated by SPM and not by soliton fission, even the structure at 1900 nm cannot be considered a soliton although it is located in the anomalous dispersion region. The spectrogram clearly shows a chirp across its spectrum, while a soliton would exhibit a flat spectral phase. The non-formation of a soliton can be understood by considering nonlinear and dispersive length scales [53]. While $L_{NL} < 2$ cm, L_D is in the order of 2.5 m. Soliton formation requires a certain balance of dispersion and nonlinearity [53], which is not given in our conditions. Hence, although the fiber does not strictly exhibit an ANDi profile, the SC pulse should possess the typical low-noise, high stability properties usually associated with ANDi SC generation [2,3].

6. Conclusions

We reported the detailed experimental spectro-temporal characterization of coherent SC pulses from all-solid silicate glass and silica/Ge:silica core microstructure PCF. Both PM and non-PM fibers investigated in this work are pumped by a commercial ultrafast Er:fiber amplifier system. We used TDP to reconstruct the measured spectrograms of the SC pulses. Our measurements revealed that the SC pulses investigated in ANDi PCF exhibit intricate pulse shapes. Using e-PIE we retrieved a considerable amount of temporal fine structure and fast oscillations on the scale of tens of femtoseconds. Simulations also related the origin of the complex SC features to imperfections of the input pump pulse, such as side pulses and low-level pedestals, which are common in high energy femtosecond Er:fiber amplifier systems. In addition, we observed spectro-temporal structures in weakly birefringent fiber samples that are consistent with signatures of incoherent noise amplification discussed in recent numerical studies [3,38]. These results give important guidelines for the construction of high quality ANDi SC sources for application in ultrafast photonics.

We have confirmed that positively and near-linearly chirped pulses are readily available from different structures of lead-silicate soft glass fibers, including variants that are PM. Here we extended this work with results on silica/Ge-doped silica PM fibers, which served to confirm that similar characteristics can be obtained from fusion splicing-compatible fibers. However, engineering of flat, ANDi profiles in silica fibers across both near-infrared gain bands of trivalent erbium and thulium ions is challenging. All-solid silicate glass ANDi PCF enabling all-normal dispersion nonlinear dynamics have been demonstrated in coherent, broadband seeding of ultrafast Tm-doped fiber amplifiers [17–19]. Application of the redshifted OWB spectral wing of the ANDi SC in these systems as the seed signal allowed relative intensity noise performance exceeding previous demonstrations of soliton-seeded amplifiers by an order of magnitude.

Funding

Schweizerischer Nationalfonds zur Förderung der Wissenschaftlichen Forschung (PCEFP2_181222); Fundacja na rzecz Nauki Polskiej (First TEAM/2016-1/1 - POIR.04.04.00-00-1D64/16-00).

Acknowledgments

Anupamaa Rampur received support from the Schlumberger Foundation Faculty for the Future program.

Disclosures

The authors declare no conflicts of interest.

Data availability

The raw data for the significant figures in this paper is available online at <http://dx.doi.org/10.7892/boris.143434>.

References

1. F. W. Wise, A. Chong, and W. H. Renninger, "High-energy femtosecond fiber lasers based on pulse propagation at normal dispersion," *Laser Photonics Rev.* **2**(1-2), 58–73 (2008).
2. A. M. Heidt, A. Hartung, and H. Bartelt, "The Supercontinuum Laser Source: The Ultimate White Light," in (Springer, New York, 2016), pp. 247–280.
3. A. M. Heidt, J. S. Feehan, J. H. v. Price, and T. Feurer, "Limits of coherent supercontinuum generation in normal dispersion fibers," *J. Opt. Soc. Am. B* **34**(4), 764–775 (2017).
4. K. L. Corwin, N. R. Newbury, J. M. Dudley, S. Coen, S. A. Diddams, K. Weber, and R. S. Windeler, "Fundamental Noise Limitations to Supercontinuum Generation in Microstructure Fiber," *Phys. Rev. Lett.* **90**(11), 113904 (2003).
5. A. M. Heidt, A. Hartung, G. W. Bosman, P. Krok, E. G. Rohwer, H. Schwoerer, and H. Bartelt, "Coherent octave spanning near-infrared and visible supercontinuum generation in all-normal dispersion photonic crystal fibers," *Opt. Express* **19**(4), 3775 (2011).
6. S. Demmler, J. Rothhardt, A. M. Heidt, A. Hartung, E. G. Rohwer, H. Bartelt, J. Limpert, and A. Tünnermann, "Generation of high quality, 1.3 cycle pulses by active phase control of an octave spanning supercontinuum," *Opt. Express* **19**(21), 20151 (2011).
7. J. Rothhardt, S. Demmler, S. Hädrich, J. Limpert, and A. Tünnermann, "Octave-spanning OPCPA system delivering CEP-stable few-cycle pulses and 22 W of average power at 1 MHz repetition rate," *Opt. Express* **20**(10), 10870 (2012).
8. J. Rothhardt, S. Hädrich, J. C. Delagnes, E. Cormier, and J. Limpert, "High Average Power Near-Infrared Few-Cycle Lasers," *Laser Photonics Rev.* **11**(4), 1700043 (2017).
9. H. Tu and S. A. Boppart, "Coherent fiber supercontinuum for biophotonics," *Laser Photonics Rev.* **7**(5), 628–645 (2013).
10. H. Tu and S. A. Boppart, "Coherent anti-Stokes Raman scattering microscopy: overcoming technical barriers for clinical translation," *J. Biophotonics* **7**(1-2), 9–22 (2014).
11. N. Nishizawa, "Wideband ultrafast fiber laser sources for OCT and metrology," *J. Phys. B: At., Mol. Opt. Phys.* **49**(18), 182003 (2016).
12. N. M. Kearns, A. C. Jones, M. B. Kunz, R. T. Allen, J. T. Flach, and M. T. Zanni, "Two-dimensional white-light spectroscopy using supercontinuum from an all-normal dispersion photonic crystal fiber pumped by a 70 MHz Yb fiber oscillator," *J. Phys. Chem. A* **123**(13), 3046–3055 (2019).
13. Y. Wang, S. Dai, G. Li, D. Xu, C. You, X. Han, P. Zhang, X. Wang, and P. Xu, "1.4–7.2 μm broadband supercontinuum generation in an As-S chalcogenide tapered fiber pumped in the normal dispersion regime," *Opt. Lett.* **42**(17), 3458–3461 (2017).
14. N. Zhang, X. Peng, Y. Wang, S. Dai, Y. Yuan, J. Su, G. Li, P. Zhang, P. Yang, and X. Wang, "Ultrabroadband and coherent mid-infrared supercontinuum generation in Te-based chalcogenide tapered fiber with all-normal dispersion," *Opt. Express* **27**(7), 10311–10319 (2019).
15. S. Rao D. S., S. D. Engelsholm, I. B. Gonzalo, B. Zhou, P. Bowen, P. M. Moselund, O. Bang, and M. Bache, "Ultra-low-noise supercontinuum generation with a flat near-zero normal dispersion fiber," *Opt. Lett.* **44**(9), 2216 (2019).
16. K. Tarnowski, T. Martynkien, P. Mergo, J. Sotor, and G. Soboń, "Compact all-fiber source of coherent linearly polarized octave-spanning supercontinuum based on normal dispersion silica fiber," *Sci. Rep.* **9**(1), 12313 (2019).
17. J. M. Hodasi, A. Heidt, M. Klimczak, B. Siwicki, and T. Feurer, "Femtosecond seeding of a Tm-Ho fiber amplifier by a broadband coherent supercontinuum pulse from an all-solid all-normal photonic crystal fiber," in *2017 European*

- Conference on Lasers and Electro-Optics and European Quantum Electronics Conference* (Optical Society of America, 2017), p. CJ_P_7.
18. A. M. Heidt, J. Modupeh Hodasi, A. Rampur, D.-M. Spangenberg, M. Ryser, M. Klimczak, and T. Feurer, "Low noise all-fiber amplification of a coherent supercontinuum at 2 μm and its limits imposed by polarization noise," arXiv e-prints arXiv:1903.09583 (2019).
 19. A. Rampur, Y. Stepanenko, G. Stępniewski, T. Kardaś, D. Dobrakowski, D.-M. Spangenberg, T. Feurer, A. Heidt, and M. Klimczak, "Ultra low-noise coherent supercontinuum amplification and compression below 100 fs in an all-fiber polarization-maintaining thulium fiber amplifier," *Opt. Express* **27**(24), 35041 (2019).
 20. A. M. Heidt, "Pulse preserving flat-top supercontinuum generation in all-normal dispersion photonic crystal fibers," *J. Opt. Soc. Am. B* **27**(3), 550–559 (2010).
 21. A. Hartung, A. M. Heidt, and H. Bartelt, "Nanoscale all-normal dispersion optical fibers for coherent supercontinuum generation at ultraviolet wavelengths," *Opt. Express* **20**(13), 13777–13788 (2012).
 22. T. S. Saini, N. P. T. Hoa, T. H. Tuan, X. Luo, T. Suzuki, and Y. Ohishi, "Tapered tellurite step-index optical fiber for coherent near-to-mid-IR supercontinuum generation: experiment and modeling," *Appl. Opt.* **58**(2), 415–421 (2019).
 23. E. Genier, P. Bowen, T. Sylvestre, J. M. Dudley, P. Moselund, and O. Bang, "Amplitude noise and coherence degradation of femtosecond supercontinuum generation in all-normal-dispersion fibers," *J. Opt. Soc. Am. B* **36**(2), A161 (2019).
 24. J. Szczepanek, T. M. Kardaś, and Y. Stepanenko, "Group delay measurements of ultra-broadband pulses generated in highly nonlinear fibers," *Photonics Lett. Pol.* **8**(4), 107–109 (2016).
 25. A. Okamura, Y. Sakakibara, E. Omoda, H. Kataura, and N. Nishizawa, "Experimental analysis of coherent supercontinuum generation and ultrashort pulse generation using cross-correlation frequency resolved optical gating (X-FROG)," *J. Opt. Soc. Am. B* **32**(3), 400–406 (2015).
 26. K. Tarnowski, T. Martynkien, P. Mergo, K. Poturaj, G. Soboń, and W. Urbańczyk, "Coherent supercontinuum generation up to 2.2 μm in an all-normal dispersion microstructured silica fiber," *Opt. Express* **24**(26), 30523 (2016).
 27. J. M. Dudley, X. Gu, L. Xu, M. Kimmel, E. Zeek, P. O'Shea, R. Trebino, S. Coen, and R. S. Windeler, "Cross-correlation frequency resolved optical gating analysis of broadband continuum generation in photonic crystal fiber: simulations and experiments," *Opt. Express* **10**(21), 1215 (2002).
 28. S. Dupont, P. M. Moselund, L. Leick, J. Ramsay, and S. R. Keiding, "Up-conversion of a megahertz mid-IR supercontinuum," *J. Opt. Soc. Am. B* **30**(10), 2570–2575 (2013).
 29. J. C. Travers, "Blue solitary waves from infrared continuous wave pumping of optical fibers," *Opt. Express* **17**(3), 1502 (2009).
 30. Y. Shen, A. A. Voronin, A. M. Zheltikov, S. P. O'Connor, V. v. Yakovlev, A. v. Sokolov, and M. O. Scully, "Picosecond supercontinuum generation in large mode area photonic crystal fibers for coherent anti-Stokes Raman scattering microspectroscopy," *Sci. Rep.* **8**(1), 9526 (2018).
 31. J. Vengelis, V. Jarutis, and V. Sirutkaitis, "Estimation of photonic crystal fiber dispersion by means of supercontinuum generation," *Opt. Lett.* **42**(9), 1844 (2017).
 32. T. C. Wong, M. Rhodes, and R. Trebino, "Single-shot measurement of the complete temporal intensity and phase of supercontinuum," *Optica* **1**(2), 119 (2014).
 33. D. Spangenberg, P. Neethling, E. Rohwer, M. H. Brüggmann, and T. Feurer, "Time-domain ptychography," *Phys. Rev. A* **91**(2), 021803 (2015).
 34. M. Lucchini, M. H. Brüggmann, A. Ludwig, L. Gallmann, U. Keller, and T. Feurer, "Ptychographic reconstruction of attosecond pulses," *Opt. Express* **23**(23), 29502–29513 (2015).
 35. A. M. Heidt, D.-M. Spangenberg, M. Brüggmann, E. G. Rohwer, and T. Feurer, "Improved retrieval of complex supercontinuum pulses from XFROG traces using a ptychographic algorithm," *Opt. Lett.* **41**(21), 4903 (2016).
 36. T. Witting, D. Greening, D. Walke, P. Matia-Hernando, T. Barillot, J. P. Marangos, and J. W. G. Tisch, "Time-domain ptychography of over-octave-spanning laser pulses in the single-cycle regime," *Opt. Lett.* **41**(18), 4218–4221 (2016).
 37. D. Brida, G. Krauss, A. Sell, and A. Leitenstorfer, "Ultrabroadband Er: fiber lasers," *Laser Photonics Rev.* **8**(3), 409–428 (2014).
 38. I. B. Gonzalo, R. D. Engelsholm, M. P. Sørensen, and O. Bang, "Polarization noise places severe constraints on coherence of all-normal dispersion femtosecond supercontinuum generation," *Sci. Rep.* **8**(1), 6579 (2018).
 39. P. Ciącka, A. Rampur, A. Heidt, T. Feurer, and M. Klimczak, "Dispersion measurement of ultra-high numerical aperture fibers covering thulium, holmium, and erbium emission wavelengths," *J. Opt. Soc. Am. B* **35**(6), 1301–1307 (2018).
 40. P. Hlubina, M. Kadulová, and D. Ciprian, "Spectral interferometry-based chromatic dispersion measurement of fibre including the zero-dispersion wavelength," *JEOS:RP* **7**, 12017 (2012).
 41. M. Klimczak, B. Siwicki, B. Zhou, M. Bache, D. Pysz, O. Bang, and R. Buczyński, "Coherent supercontinuum bandwidth limitations under femtosecond pumping at 2 μm in all-solid soft glass photonic crystal fibers," *Opt. Express* **24**(26), 29406 (2016).
 42. M. Klimczak, B. Siwicki, P. Skibiński, D. Pysz, R. Stępień, A. Heidt, C. Radzewicz, and R. Buczyński, "Coherent supercontinuum generation up to 2.3 μm in all-solid soft-glass photonic crystal fibers with flat all-normal dispersion," *Opt. Express* **22**(15), 18824–18832 (2014).

43. D. Dobrakowski, A. Rampur, G. Stępniewski, A. Anuszkiewicz, J. Lisowska, D. Pysz, R. Kasztelan, and M. Klimczak, "Development of highly nonlinear polarization-maintaining fibers with normal dispersion across entire transmission window," *J. Opt.* **21**, 015504 (2019).
44. K. Tarnowski, T. Martynkien, P. Mergo, K. Poturaj, A. Anuszkiewicz, P. B  jot, F. Billard, O. Faucher, B. Kibler, and W. Urbanczyk, "Polarized all-normal dispersion supercontinuum reaching 2.5 μm generated in a birefringent microstructured silica fiber," *Opt. Express* **25**(22), 27452 (2017).
45. B. Kibler, J. M. Dudley, and S. Coen, "Supercontinuum generation and nonlinear pulse propagation in photonic crystal fiber: influence of the frequency-dependent effective mode area," *Appl. Phys. B* **81**(2-3), 337–342 (2005).
46. R. Trebino, *Frequency-Resolved Optical Gating: The Measurement of Ultrashort Laser Pulses* (Springer Science & Business Media, 2012).
47. X. Gu, L. Xu, M. Kimmel, E. Zeek, P. O'Shea, A. P. Shreenath, R. Trebino, and R. S. Windeler, "Frequency-resolved optical gating and single-shot spectral measurements reveal fine structure in microstructure-fiber continuum," *Opt. Lett.* **27**(13), 1174–1176 (2002).
48. G. Taft, A. Rundquist, M. M. Murnane, I. P. Christov, H. C. Kapteyn, K. W. DeLong, D. N. Fittinghoff, M. A. Krumbugel, J. N. Sweetser, and R. Trebino, "Measurement of 10-fs laser pulses," *IEEE J. Sel. Top. Quantum Electron.* **2**(3), 575–585 (1996).
49. K. W. DeLong and R. Trebino, "Improved ultrashort pulse-retrieval algorithm for frequency-resolved optical gating," *J. Opt. Soc. Am. A* **11**(9), 2429–2437 (1994).
50. J. M. Dudley, G. Genty, and S. Coen, "Supercontinuum generation in photonic crystal fiber," *Rev. Mod. Phys.* **78**(4), 1135–1184 (2006).
51. A. A. Rieznik, A. M. Heidt, P. G. Konig, V. A. Bettachini, and D. F. Grosz, "Optimum Integration Procedures for Supercontinuum Simulation," *IEEE Photonics J.* **4**(2), 552–560 (2012).
52. G. Millot, E. Seve, S. Wabnitz, and M. Haelterman, "Observation of induced modulational polarization instabilities and pulse-train generation in the normal-dispersion regime of a birefringent optical fiber," *J. Opt. Soc. Am. B* **15**(4), 1266 (1998).
53. G. P. Agrawal, *Nonlinear Fiber Optics* (Academic Press, 2007).